Incorporating non-equilibrium effects in an ODE-based wall model

By K. P. Griffin, L. Fu AND P. Moin

1. Motivation and objectives

The accurate prediction of wall-bounded turbulence is of practical importance for many engineering applications, e.g., the design of low-drag vehicles. While direct numerical simulation (DNS) and large-eddy simulation (LES) are capable of delivering accurate solutions, the required number of grid points scales with $Re^{2.05}$ (Yang & Griffin 2020) and $Re^{1.86}$ (Choi & Moin 2012), respectively, rendering them prohibitively expensive for high-Reynolds-number flows. Alternatively, the computational cost of the wall-modeled LES (WMLES) approach, which resolves the large-scale energetic motion in the outer portion of the boundary layer and employs a reduced-order model for the near-wall turbulence, scales only linearly with Reynolds number (Choi & Moin 2012). Because the LES subgrid-scale model itself typically provides an inconsistent wall shear stress when the near-wall turbulent eddies are poorly resolved, the performance of WMLES relies heavily on the wall model. The main wall models include wall-stress-based models (Deardorff *et al.* 1970; Bose & Park 2018; Larsson *et al.* 2016), the detached-eddy simulation (DES) paradigm (Spalart 2009), the dynamic-slip wall model (Bose & Moin 2014; Bae *et al.* 2019; Griffin *et al.* 2018, 2019), integral-based models (Yang *et al.* 2015), and other variants. In this work, our discussion is restricted to the wall-stress-based models, and readers are referred to Bose & Park (2018) for a more comprehensive review on other wall models.

Most ordinary differential equation (ODE)-based wall-stress models are strictly valid only for equilibrium flows, which feature a constant edge condition such as fully developed pipe or channel flows, and zero pressure gradient boundary layer (ZPGBL) flows. Conversely, a non-equilibrium flow is characterized by an edge condition that is non-constant and evolves spatially. To simulate such a flow, the natural choice is to solve the full boundary-layer partial differential equations (PDEs) as a wall-stress-based model such that some non-equilibrium effects can be captured (Balaras *et al.* 1996; Park & Moin 2014; Wang & Moin 2002; Kawai & Larsson 2013). The main disadvantages of solving the boundary layer PDEs lie in the significantly increased computational cost and the requirement of a high-quality near-wall mesh, which is non-trivial to generate for complex geometries.

ODE-based non-equilibrium wall models have been proposed by augmenting equilibrium models with some of the typically neglected terms in the full boundary layer PDEs, e.g., Hoffmann & Benocci (1995), Wang & Moin (2002), Catalano *et al.* (2003), Duprat *et al.* (2011), and Chen *et al.* (2014). However, these models have had limited success since they typically rely on eddy viscosity models that have not been adapted to accommodate the added terms in the models, as argued by Griffin & Fu (2020). In fact, often the equilibrium model performs better than these ODE-based non-equilibrium models (Hickel *et al.* 2013).

The core concept of the equilibrium wall model is that it assumes that the mean

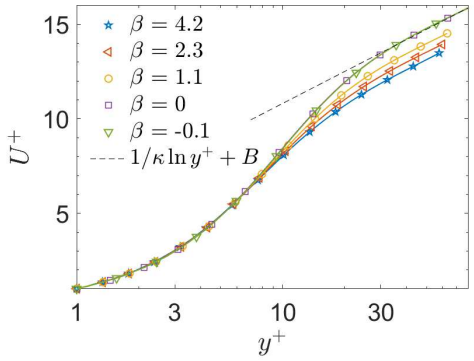

FIGURE 1. The distribution of the mean streamwise velocity U^+ plotted versus the wall-normal coordinate y^+ for five cases from Table 1. Included are three adverse pressure gradient boundary layers (APGBLs) ($\beta = 4.2, 2.3, 1.1$), a ZPGBL at $Re_\tau = \delta u_\tau/\nu = 2000$ ($\beta = 0$), and a channel flow at $Re_\tau = 5200$ ($\beta = -0.1$). Also plotted is the reference log law distribution with the Kármán constant $\kappa = 0.41$ and the intercept constant $B = 5.2$. All data are truncated at $y = 0.1\delta$, which approximately encompasses the viscous sublayer, buffer layer, and log layer.

velocity profile exhibits a logarithmic region, which is said to obey the log law, i.e.,

$$U^+ = \frac{1}{\kappa} \ln(y^+) + B, \tag{1.1}$$

where the parameter $1/\kappa$ denotes the log slope and B denotes the log intercept constant. Throughout the following discussions, the superscript + refers to quantities non-dimensionalized via the viscous length scale $\delta_v = \nu/u_\tau$ and the velocity scale u_τ. The equilibrium model is calibrated with a particular choice of κ and B. The validity of this assumption in non-equilibrium flows is evaluated in Figure 1, where pressure gradient flows are compared with a ZPGBL. Clearly, the log law persists even in the presence of moderate pressure gradients indicated by the outer pressure gradient parameter $\beta = (\delta^*/\tau_w)\mathrm{d}P/\mathrm{d}x$. The log intercept constant B exhibits non-universality, and the calibration of the equilibrium model using the log law observed in the equilibrium case of $\beta = 0$ leads to a 17% underprediction of the wall shear stress for the non-equilibrium case with $\beta = 4.2$, as will be discussed in Section 4. This underprediction motivates the present approach in which the log-law intercept implicitly depends on the friction Reynolds number and the outer velocity field (through the shape factor) to incorporate the history effects from the outer PDE solver into the ODE-based wall model.

To facilitate the deployment of the wall model in complex applications, a new method for determining the boundary-layer thickness is also presented. As a result, the proposed wall model greatly extends the predictive capability of the ODE-based wall model for flows with strong pressure gradients and a wide range of Reynolds numbers.

This remainder of this report is organized as follows. In Section 2, a new model accounting for pressure gradient and Reynolds number effects is presented. In Section 3, a method for determining the boundary-layer thickness in complex flows is presented. In Section 4, these two methods are integrated and their performance is validated for predicting the wall stress in a wide range of flows. In Section 5, concluding discussions and remarks are given.

Type of flow	Re_τ	β	H	Number of profiles
ZPGBLs	[276,2479]	[0.00, 0.00]	[1.36,1.49]	8
Channels	[543,5186]	[-0.13,-0.10]	[1.25,1.40]	4
Pipes	[685,1143]	[-0.28,-0.28]	[1.37,1.40]	2
APGBLs	[202, 740]	[0.19, 4.43]	[1.56,1.91]	21
NACA 0012 AoA = 0°	[264, 371]	[0.30, 1.71]	[1.55,1.59]	3
NACA 4412 AoA = 5°	[290, 679]	[-0.14, 2.08]	[1.41,1.59]	8

TABLE 1. Well-resolved simulation database from various types of flows for wall model evaluation. Included are ZPGBLs (Sillero *et al.* 2013; Spalart 1988; Eitel-Amor *et al.* 2014), fully developed channel (Lee & Moser 2015) and pipe (Wu & Moin 2008) flows, APGBLs with five different pressure gradient conditions (Bobke *et al.* 2017), and two airfoil flows with specified angle of attack (AoA) (Tanarro *et al.* 2020; Vinuesa *et al.* 2018). The ranges of friction Reynolds number Re_τ, the outer pressure-gradient parameter $\beta = (\delta^*/\tau_w)\mathrm{d}P/\mathrm{d}x$, and the boundary-layer shape factor H are also provided, as well as the number of 1D profiles available for each flow.

2. ODE-based non-equilibrium wall model

The present model is developed by Griffin & Fu (2020) and is summarized below. Like the classical equilibrium wall model, this model begins by rearranging the definition of the total shear stress as an ODE for the mean streamwise velocity profile and non-dimensionalizing with respect to the inner units u_τ and δ_v, i.e.,

$$\frac{\mathrm{d}U^+}{\mathrm{d}y^+} = \frac{\tau^+}{1+\nu_t^+}. \tag{2.1}$$

While classical equilibrium wall models (Prandtl 1925; Cabot 1995) proceed by invoking the constant-stress-layer assumption $\tau^+ = \tau/\tau_w \approx 1$ and a damped linear mixing length assumption for the eddy viscosity, the present approach avoids the independent modeling of the stress and the eddy viscosity profiles by directly parameterizing the mean shear as

$$\frac{\mathrm{d}U^+}{\mathrm{d}y^+} = \frac{1}{1+\ell_n^+}, \tag{2.2}$$

where ℓ_n^+ is introduced as an empirical function and is defined as

$$\ell_n^+ = \frac{1-\tau^+ + \nu_t^+}{\tau^+}, \tag{2.3}$$

so that Eq. (2.2) is exactly equivalent to Eq. (2.1). By analogy to Cabot's model, ℓ_n^+ is referred to as a non-dimensional mixing length. The new mixing length is equivalent to Cabot's in the special case of a constant stress layer, i.e., $\tau^+ \approx 1$.

To recover a log law at far wall-normal distances, ℓ_n^+ is modeled as

$$\ell_n^+ = \kappa y^+ \left(1 - \exp\left[-\left(\frac{y^+}{A^+}\right)^{2/b}\right]\right)^b, \tag{2.4}$$

where κ, b and A^+ are model coefficients. This model guarantees that the correct near-wall and log-region behavior of the eddy viscosity profile is achieved (Griffin & Fu 2020) for any choice of κ, b, and A^+. The widely used model of Cabot & Moin (2000) chooses

$\kappa = 0.41$, $b = 2$ and $A^+ = 17$. Upon integration, Cabot's model will always predict the equilibrium velocity profile in Figure 1, even when the non-equilibrium solutions are applicable.

On the other hand, the present model sets $\kappa = 0.38$, $b = 1$ and permits A^+ to depend on the outer flow so that non-equilibrium flows can be correctly captured. A^+ is a linear function of the friction Reynolds number $Re_\tau = \delta u_\tau/\nu$ and the boundary-layer shape factor H, which is defined and computed in section 3. Specifically, the damping coefficient A^+ is given by

$$A^+[H, Re_\tau] = 45.2 - 11.8H - 0.993 \ln (Re_\tau) . \tag{2.5}$$

That the log intercept depends on Re_τ is already well known (Nagib & Chauhan 2008), but neglected in classical equilibrium models. The dependence of A^+ (or after integration, B) on shape factor is a new idea (Griffin & Fu 2020). Johnstone *et al.* (2010) and Bobke *et al.* (2017) observed that measures of the local pressure gradient are insufficient for characterizing the shape of the velocity profile in pressure gradient boundary layers because these parameters are unaware of the spatial (or temporal in a Lagrangian sense) history of the flow. Meanwhile, the boundary-layer shape factor depends on the spatially evolving outer solution in a WMLES context, which contains history effects that are not captured by local pressure gradient parameters.

Note that the regression in Eq. (2.5) applies only to the present mixing length model with $b = 1$ and $\kappa = 0.38$ for fully turbulent, incompressible flows with zero wall penetration. Although the optimal choices of the regression coefficients may be different for other mixing-length models, the suitability of correlating A^+ with H and Re_τ may still hold in general.

3. Robustly computing the shape factor in complex flows

To deploy the wall model described in section 2, a robust procedure for computing the boundary-layer shape factor is required. The boundary-layer shape factor is defined as the ratio of the displacement thickness δ^* and the momentum thickness θ. Unlike in ZPGBLs, in general flows, U does not approach a constant aysmptote at the boundary-layer edge, so the classical integral definitions of δ^* and θ will not converge unless they are truncated at the boundary-layer edge $y = \delta$. Specifically, the displacement thickness is defined as

$$\delta^* = \int_0^\delta \left(1 - \frac{U}{U_e}\right) dy, \tag{3.1}$$

and the momentum thickness is defined as

$$\theta = \int_0^\delta \frac{U}{U_e}\left(1 - \frac{U}{U_e}\right) dy, \tag{3.2}$$

where $U_e = U[y = \delta]$ denotes the boundary-layer edge velocity. In this manner, only the viscous region contributes to δ^* and θ. The boundary-layer shape factor is defined as $H = \delta^*/\theta$.

The computation of H then relies on a robust method for determining δ in general flows. In this section, a new method for defining δ based on stagnation pressure is described.

3.1. *New approach for computing the boundary-layer thickness*

Griffin *et al.* (2020) present a new method for computing the boundary-layer thickness,

and it is briefly summarized below. The boundary-layer thickness δ_n, where n is typically taken to be 99, is defined as

$$\frac{U}{U_I}\Big|_{y=\delta_n} = \frac{n}{100}, \tag{3.3}$$

where $U_I[y]$ denotes a local reconstruction of the inviscid mean streamwise velocity profile. This new method is a generalization of the classical ZPGBL definition for δ_n, $U/U_\infty|_{y=\delta_n} = n/100$, where $U_\infty = U[y \to \infty]$. The two definitions are equivalent for a ZPGBL, where the inviscid solution is simply a constant, i.e., $U_I[y] = U_\infty$.

Formally, the inviscid velocity profile can be obtained by solving the Euler equations and imposing no-penetration boundaries contoured to the local displacement thickness computed in a viscous simulation. However, since the displacement thickness depends on the boundary-layer thickness, this approach is impractical. On the other hand, in this work, a simpler and more computationally efficient local reconstruction of the inviscid solution $U_I[y]$ is proposed. This approach begins by defining the stagnation pressure for an incompressible steady flow as

$$P_o = P + \frac{1}{2}\rho U_m^2, \tag{3.4}$$

where P is the static pressure and the velocity magnitude squared $U_m^2 = U_I^2 + V^2$ is computed from the reconstructed mean streamwise velocity U_I and the mean wall-normal velocity V in the 2D local reference frame.

While the no-penetration boundary condition, i.e., $V[y = 0] = 0$, applies for both inviscid and viscous flows, the no-slip boundary condition, i.e., $U[y = 0] = 0$, applies only to viscous flows. As a result, the reconstructed inviscid mean streamwise velocity profile $U_I[y]$ deviates from $U[y]$ near the wall, where the viscous effects dominate. Meanwhile, the wall-normal velocity profile $V[y]$ and the mean pressure profile $P[y]$ feature a much weaker dependence on viscous effects. For a flat-plate pressure-gradient boundary layer, $\partial P/\partial y \approx 0$ and $V \approx 0$ in both the viscous and the inviscid cases.

Considering a hypothetical irrotational, inviscid flow that has $V[y]$ and $P[y]$ profiles equivalent to those of the corresponding viscous flow, the Bernoulli equation may approximately apply globally rather than just along streamlines. Therefore, the corresponding streamwise velocity $U_I[y]$ is obtained from Bernoulli's equation following

$$U_I = \pm\sqrt{\frac{2}{\rho}\left(P_{o,ref} - P[y]\right) - V^2[y]}, \tag{3.5}$$

where $P_{o,ref}$ denotes the total pressure at a reference location specified below. The sign of U_I can be chosen to match that of U.

The rationale is that the viscous effects are approximately confined to the boundary layer, i.e., the flow is nearly inviscid and irrotational outside of the boundary layer with $y > \delta$. This implies that $P_{o,ref}$ is nearly a constant across the domain with $y > \delta$. Taking the flow over an airfoil for instance, as shown in Figure 2a, the dynamic pressure varies continuously, whereas the stagnation pressure preserves a constant asymptote outside of the boundary layer. Meanwhile, one unique choice of $P_{o,ref}$ is given by setting $P_{o,ref} = \max(P_o)$, which is achieved at a wall-normal distance $y > \delta$. Since P_o is a measure of the flow's capacity to do work, it typically decreases as a wall is approached. This choice of $P_{o,ref}$ guarantees that the model has the correct behavior in channel and pipe flows.

The locally reconstructed inviscid solution $U_I[y]$ given by Eq. (3.5) is plotted for the flow over a NACA 4412 airfoil (Vinuesa *et al.* 2018) in Figure 2b. As expected, the

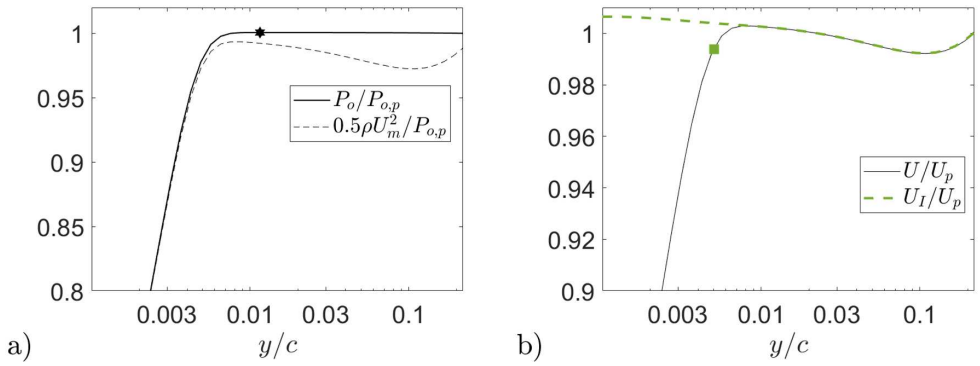

FIGURE 2. Distributions of the stagnation pressure P_o and the dynamic pressure $0.5\rho U_m^2$ (a), and the mean velocity U and the locally reconstructed inviscid solution U_I (b) versus the wall-normal coordinate y for the pressure side of a NACA 4412 airfoil at AoA $= 5^\circ$ and $Re_c = 10^6$ detailed in Table 1. All data are from the streamwise location $x/c = 0.21$. The maximum stagnation pressure (a) and estimates of the boundary-layer edges from the respective methods (b) are plotted with symbols. The subscript p denotes quantities evaluated at the furthest point from the wall in the wall-normal profile.

inviscid solution $U_I[y]$ has an excellent agreement with the viscous solution $U[y]$ outside the boundary layer. The boundary-layer thickness δ_{99} is then estimated to be the location where U_I departs from U by one percent. In this work, the boundary-layer edge velocity is taken to be $U_e = U[y = \delta_{99}]$.

Note that, in experiments and coarse simulations alike, small spurious oscillations in the velocity profile can occur. For this reason, the search for $U/U_I = n/100$ should begin at the wall and proceed in the wall-normal direction. Selecting $n < 99$ may be appropriate for poorly converged data.

3.2. *Performance of methods for computing the boundary-layer thickness*

The new method for computing δ is compared with the following four existing methods.

(i) The approach of Coleman *et al.* (2018) determines δ_n by finding the wall-normal distance at which

$$\frac{\widetilde{U}}{\widetilde{U}_\infty}\Big|_{y=\delta_n} = \frac{n}{100}, \tag{3.6}$$

where $\widetilde{U} = \int_0^y -\Omega_z dy'$ and $\Omega_z = \partial V/\partial x - \partial U/\partial y$ denotes the mean spanwise vorticity. This approach is referred to as the $\widetilde{U}_\infty$ method hereafter.

(ii) In the approach of Uzun & Malik (2020), a threshold for $-y\Omega_z$ is empirically connected to the desired δ_n, i.e.,

$$\frac{-y\Omega_z}{\max(-y\Omega_z)}\Big|_{y=\delta_n} = C_\Omega, \tag{3.7}$$

where C_Ω is an empirical parameter that depends on the choice of n. For instance, for δ_{99}, $C_\Omega = 0.02$ is suggested (Uzun & Malik 2020). This approach is henceforth referred to as the $-y\Omega_z$ threshold method.

(iii) In the mean-shear-based methods, the boundary-layer thickness δ is defined as the wall-normal distance y, where the mean shear $\partial U/\partial y$ drops below an arbitrary threshold.

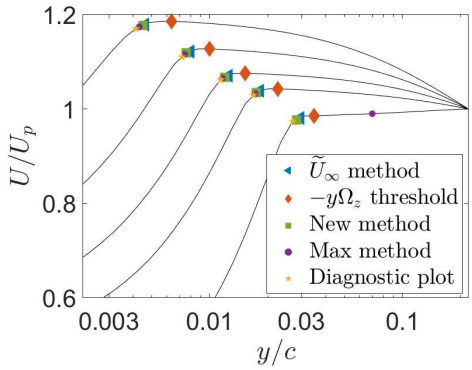

FIGURE 3. Distributions of the mean streamwise velocity (black solid lines) versus the wall-normal coordinate y for various profiles from the suction side of a NACA 4412 at AoA = 5° and $Re_c = 10^6$ detailed in Table 1. These wall-normal profiles originate from the airfoil surface at the streamwise stations $x/c = 0.20, 0.37, 0.55, 0.72, 0.90$ (from top-left to bottom-right). The estimates of the boundary-layer edges (and the corresponding edge velocities) are plotted with symbols as indicated in the legend. The subscript p denotes quantities evaluated at the furthest point from the wall in the wall-normal profile.

A special case of this method, henceforth referred to as the max method, is when the threshold is set to be zero, such that $y = \delta$ occurs at the maximum of $U[y]$.

(iv) Drózdz *et al.* (2015) assert that a plot of $\sqrt{\overline{u'^2}}/(U_e\sqrt{H})$ versus U/U_e becomes nearly universal as $y \to \delta$; this plot is referred to as a diagnostic plot. Based on its observed asymptotic behavior, Vinuesa *et al.* (2016) define the boundary-layer edge δ_{99} as the wall-normal distance at which $\sqrt{\overline{u'^2}}/(U_e\sqrt{H}) = 0.02$. Note that since the criterion for determining δ depends on the boundary-layer edge velocity U_e, an iterative procedure and an appropriate initial guess for δ are required.

Since there is no established definition for the boundary-layer thickness δ in complex flows, it is challenging to quantitatively assess the performance of various methods. On the other hand, in many scenarios, a qualitative examination is important and sufficient for turbulence model development.

Considering the flow over the suction side of a NACA 4412 airfoil at the AoA = 5° and the Reynolds number based on the chord length $Re_c = 10^6$, Figure 3 shows the estimates for δ_{99} from the five previously discussed methods at five different streamwise stations. Note that the results from the $\widetilde{U}_\infty$ method, the diagnostic-plot method, and the new method are mutually consistent. The results from the max method, as the special case of the mean-shear threshold method with the threshold constant of zero, are also consistent, except at the most downstream station where the velocity profile is monotonically increasing. Meanwhile, the $-y\Omega_z$ threshold method systematically predicts a boundary-layer thickness larger than the others, implying that the threshold suggested by Uzun & Malik (2020) is not optimal for this case.

On the contrary, for the flow over the pressure side of the NACA 4412 airfoil at AoA = 5° and Reynolds number $Re_c = 10^6$, the conclusions are quite different. As shown in Figure 4, only the results from the diagnostic plot method and the new method are equivalent. Qualitatively, these methods seem to identify the boundary-layer edge in a manner that is consistent both between the five considered profiles and the predictions in Figure 3. On the other hand, the $\widetilde{U}_\infty$ method severely underpredicts δ_{99} at the most

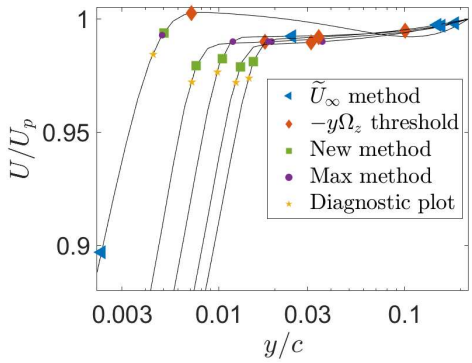

FIGURE 4. Distributions of the mean streamwise velocity (black solid lines) versus the wall-normal coordinate y for various profiles from of a NACA 4412 at AoA $= 5^\circ$ and $Re_c = 10^6$. This is the same as Figure 3 except that included profiles are from the pressure side of the airfoil (see Table 1 for details) and the wall-normal profiles originate from the airfoil surface at the streamwise stations $x/c = 0.21, 0.37, 0.54, 0.72, 0.89$ (from left to right). The estimates of the boundary-layer edges (and the corresponding edge velocities) are plotted with symbols as indicated in the legend. The subscript p denotes quantities evaluated at the furthest point from the wall in the wall-normal profile.

upstream station and overpredicts δ_{99} at other stations. The $-y\Omega_z$ threshold method also overestimates δ_{99}. As expected, the max method is unreliable, since several of the profiles are monotonically increasing and their maxima lie at y_p, the furthest point from the wall in the wall-normal profile, which is a length scale that is not intrinsically connected to the boundary-layer thickness.

In summary, the new method to identify the boundary-layer thickness (i) does not require numerical integration, numerical differentiation, or empirical thresholds; (ii) has a guaranteed solution without resorting to an iterative procedure; (iii) is applicable at all Reynolds numbers for internal and external flows with or without freestream turbulence; and (iv) only relies on the mean velocity profiles $U[y]$ and $V[y]$, and the mean pressure profile $P[y]$ as inputs. Using this method, H and Re_τ are readily computed from their definitions.

4. Wall model results

Combining the wall model presented in Section 2 with the method for computing the shape factor outlined in Section 2, the wall stress predictions are obtained for the complete range of test cases detailed in Table 1.

The new ODE model is solved iteratively in the same way as for the classical equilibrium wall models. Specifically, the no-slip boundary condition is imposed at $y = 0$, whereas the Dirichlet boundary condition $U = U_m$ is applied at the matching location $y = y_m$, where U_m is taken from the outer PDE solver. And, the matching location is typically chosen to be the first- or third-grid point of the mesh for the outer PDE solver (Yang *et al.* 2017; Kawai & Larsson 2012).

In this work, $y_m = 0.1\delta$ is adopted as suggested in Kawai & Larsson (2012). In this *a priori* study, the data at the matching location will be provided from DNS or WRLES, such that any resulting errors can be attributed to the wall model instead of to the

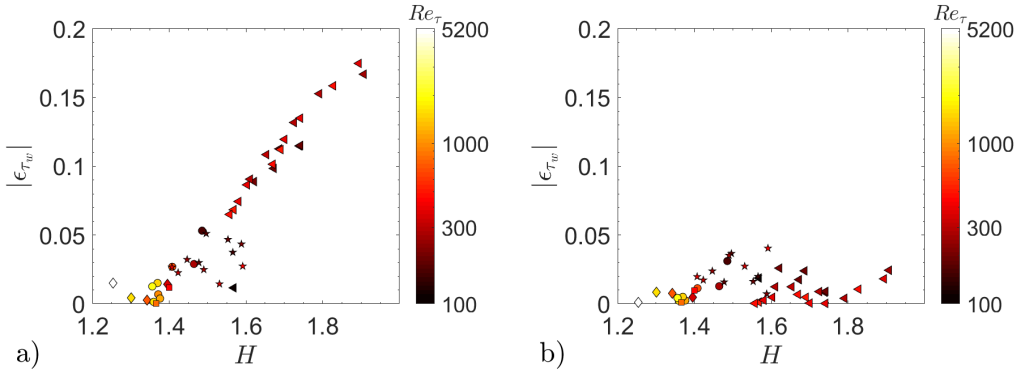

FIGURE 5. Distributions of the relative error ϵ_{τ_w} between the wall stress predicted by the well-resolved simulations and that by the wall-modeled simulations (from Cabot's model (a) and the present new model (b)) for the cases in Table 1 versus the underlying shape factor H. In both panels, the symbols denote the data from the cases in Table 1, with the symbol color indicating Re_τ and the symbol type indicating the flow type, i.e., channel flows (diamonds), ZPGBLs (circles), pipe flows (squares), APGBLs (triangles), and airfoil flows (pentagrams).

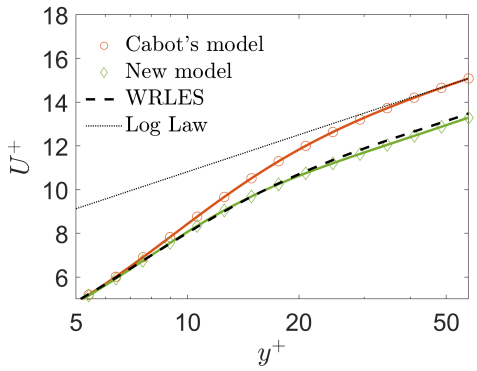

FIGURE 6. The streamwise velocity profile U^+ plotted versus the wall-normal coordinate y^+, for the $\beta = 4.2$ case considered in Figure 1. Included are the WRLES prediction (dashed line), the results from the new model (green circles) and the Cabot's model (red circles), and the log law reference (dotted line).

matching data. Here, the relative error ϵ_{τ_w} is defined as the difference between the wall shear stress τ_w computed from the wall model and that from DNS or WRLES.

As shown in Figure 5a, the relative error of the wall shear stress from the classical Cabot's model is as large as 17% for cases with strong pressure gradients. Meanwhile, the error from the new model, as shown in Figure 5b, is typically less than 2%, with a maximum of 5%. Cases with the strongest pressure gradients have the largest errors for the classical model and the most remarkable error reductions by switching to the new model. For very few cases there is a tiny error increase of about 1%, which can be attributed to the fitting errors in Eq. (2.5).

In terms of the dimensionless velocity profile, as shown in Figure 6, the new model greatly improves the prediction accuracy when compared to the classical model (Cabot's model), and the shift of the logarithmic intercept highlighted in Figure 1 is well captured.

5. Conclusion

The classical equilibrium wall model is popular because it is simple to implement in practical applications, and the performance is, in general, satisfactory for high-Reynolds-number wall-bounded turbulence. However, the prediction capability is limited because the damping coefficient A^+ does not depend on the flow state. As a result, upon integration, the classical model predicts the same logarithmic intercept even in the presence of strong pressure gradients and low Reynolds numbers. Specifically, the classical models have invoked the constant-stress-layer assumption or developed approximate correlations of the shear stress profile, without making a corresponding adjustment to the eddy viscosity model, to maintain a log law. These choices are in conflict with a wide range of high-fidelity simulation data. The present model is constructed to recover the log law without the need for assumptions about or approximations of the shear stress profile.

On the other hand, whereas most classical stress-based wall models assume a universal value for the mixing length damping coefficient A^+, the new method correlates A^+ with the boundary-layer shape factor H and the friction Reynolds number Re_τ. The proposed correlation of $A^+[H, Re_\tau]$ makes a substantial improvement to the prediction of the velocity profile and the wall shear stress for a large range of Reynolds numbers and pressure gradient conditions.

The ODE-based inner model is designed to live in symbiosis with the outer PDE-based solver, which computes the velocity profile in the outer portion of the boundary layer. By feeding these data into the inner wall model, the shape factor and the wall shear stress can be accurately predicted. As a result, the new model incorporates an integral measure of the streamwise and temporal history of the flow and is accurate in non-equilibrium scenarios, while retaining similar computational efficiency as classical equilibrium models.

Acknowledgments

KG acknowledges support from the National Defense Science and Engineering Graduate Fellowship and the Stanford Graduate Fellowship. LF and PM are funded by NASA grant No. NNX15AU93A. We wish to acknowledge helpful discussions with Sanjeeb T. Bose, Ronald Chan, Adrian Lozano Duran, Javier Urzay, and Suhas Suresh Jain.

REFERENCES

Bae, H. J., Lozano-Durán, A., Bose, S. T. & Moin, P. 2019 Dynamic slip wall model for large-eddy simulation. *J. Fluid Mech.* **859**, 400-432.

Balaras, E., Benocci, C. & Piomelli, U. 1996 Two-layer approximate boundary conditions for large-eddy simulations. *AIAA J.* **34**, 1111-1119.

Bobke, A., Vinuesa, R., Örlü, R. & Schlatter, P. 2017 History effects and near equilibrium in adverse-pressure-gradient turbulent boundary layers. *J. Fluid Mech.* **820**, 667-692.

Bose, S. & Moin, P. 2014 A dynamic slip boundary condition for wall-modeled large-eddy simulation. *Phys. Fluids* **26**, 015104.

Bose, S. T. & Park, G. I. 2018 Wall-modeled large-eddy simulation for complex turbulent flows. *Annu. Rev. Fluid Mech.* **50**, 535-561.

Cabot, W. H. 1995 Large-eddy simulations with wall models. *Annual Research Briefs*, Center for Turbulence Research, Stanford University, pp. 41-50.

Cabot, W. H. & Moin, P. 2000 Approximate wall boundary conditions in the large-eddy simulation of high Reynolds number flow. *Flow, Turbul. Combust.* **63**, 269-291.

Catalano, P., Wang, M., Iaccarino, G. & Moin, P. 2003 Numerical simulation of the flow around a circular cylinder at high Reynolds numbers. *Int. J. Heat Fluid Flow* **24**, 463-469.

Chen, Z. L., Hickel, S., Devesa, A., Berland, J. & Adams, N. A. 2014 Wall modeling for implicit large-eddy simulation and immersed-interface methods. *Theor. Comput. Fluid Dyn.* **28**, 1-21.

Choi, H. & Moin, P. 2012 Grid-point requirements for large eddy simulation: Chapman's estimates revisited. *Phys. Fluids* **24**, 011702.

Coleman, G. N., Rumsey, C. L. & Spalart, P. R. 2018 Numerical study of turbulent separation bubbles with varying pressure gradient and Reynolds number. *J. Fluid Mech.* **847**, 28-70.

Deardorff, J. W. *et al.* 1970 A numerical study of three-dimensional turbulent channel flow at large Reynolds numbers. *J. Fluid Mech.* **41** (2), 453-480.

Drózdz, A., Elsner, W. & Drobniak, S. 2015 Scaling of streamwise Reynolds stress for turbulent boundary layers with pressure gradient. *Eur. J. Mech. B/Fluids* **49**, 137-145.

Duprat, C., Balarac, G., Métais, O., Congedo, P. M. & Brugière, O. 2011 A wall-layer model for large-eddy simulations of turbulent flows with/out pressure gradient. *Phys. Fluids* **23**, 015101.

Eitel-Amor, G., Örlü, R. & Schlatter, P. 2014 Simulation and validation of a spatially evolving turbulent boundary layer up to $Re_\theta = 8300$. *Int. J. Heat Fluid Flow* **47**, 57-69.

Griffin, K., Bose, S. & Moin, P. 2018 Well-posedness of the slip wall boundary conditions for the LES equations. In *Bull. Am. Phys. Soc.*

Griffin, K., Bose, S. & Moin, P. 2019 Dynamic slip wall model for compressible turbulent flows. In *Bull. Am. Phys. Soc.*

Griffin, K. P. & Fu, L. 2020 A new ODE-based turbulence wall model accounting for pressure gradient and Reynolds number effects. arXiv:2010.04097.

Griffin, K. P., Fu, L. & Moin, P. 2020 A general method for determining the boundary-layer thickness in non-equilibrium flows. arXiv:2010.14656.

Hickel, S., Touber, E., Bodart, J. & Larsson, J. 2013 A parametrized non-equilibrium wall-model for large-eddy simulations. *Int. Symp. Turbul. Shear Flow Phenomena*.

Hoffmann, G. & Benocci, C. 1995 Approximate wall boundary conditions for large eddy simulations. *Advances in Turbulence V*. Springer, Dordrecht, pp. 222-228.

Johnstone, R., Coleman, G. N. & Spalart, P. R. 2010 The resilience of the logarithmic law to pressure gradients: evidence from direct numerical simulation. *J. Fluid Mech.* **643**, 163-175.

Kawai, S. & Larsson, J. 2012 Wall-modeling in large eddy simulation: Length scales, grid resolution, and accuracy. *Phys. Fluids* **24**, 015105.

Kawai, S. & Larsson, J. 2013 Dynamic non-equilibrium wall-modeling for large eddy simulation at high Reynolds numbers. *Phys. Fluids* **25**, 015105.

Larsson, J., Kawai, S., Bodart, J. & Bermejo-Moreno, I. 2016 Large eddy simulation with modeled wall-stress: recent progress and future directions. *Mech. Eng. Rev.* **3**, 15-00418.

Lee, M. & Moser, R. D. 2015 Direct numerical simulation of turbulent channel flow up to $Re_\tau = 5200$. *J. Fluid Mech.* **774**, 395-415.

Nagib, H. M. & Chauhan, K. A. 2008 Variations of von Kármán coefficient in canonical flows. *Phys. Fluids* **20**, 101518.

Park, G. I. & Moin, P. 2014 An improved dynamic non-equilibrium wall-model for large eddy simulation. *Phys. Fluids* **26**, 015108.

Prandtl, L. 1925 7. Bericht über Untersuchungen zur ausgebildeten Turbulenz. *ZAMM-Journal Appl. Math. Mech. Angew. Math. Mech.* **5**, 136-139.

Sillero, J. A., Jiménez, J. & Moser, R. D. 2013 One-point statistics for turbulent wall-bounded flows at Reynolds numbers up to $\delta^+ =$2000. *Phys. Fluids* **25**, 105102.

Spalart, P. R. 1988 Direct simulation of a turbulent boundary layer up to $R_\theta =$ 1410. *J. Fluid Mech.* **187**, 61-98.

Spalart, P. R. 2009 Detached-eddy simulation. *Annu. Rev. Fluid Mech.* **41**, 181-202.

Tanarro, Á., Vinuesa, R. & Schlatter, P. 2020 Effect of adverse pressure gradients on turbulent wing boundary layers. *J. Fluid Mech.* **883** (A8).

Uzun, A. & Malik, M. R. 2020 Simulation of a turbulent flow subjected to favorable and adverse pressure gradients. *AIAA Aviat. Forum* 1–33.

Vinuesa, R., Bobke, A., Örlü, R. & Schlatter, P. 2016 On determining characteristic length scales in pressure-gradient turbulent boundary layers. *Phys. Fluids* **28**, 055101.

Vinuesa, R., Negi, P. S., Atzori, M., Hanifi, A., Henningson, D. S. & Schlatter, P. 2018 Turbulent boundary layers around wing sections up to Re_c=1,000,000. *Int. J. Heat Fluid Flow* **72**, 86–99.

Wang, M. & Moin, P. 2002 Dynamic wall modeling for large-eddy simulation of complex turbulent flows. *Phys. Fluids* **14**, 2043-2051.

Wu, X. & Moin, P. 2008 A direct numerical simulation study on the mean velocity characteristics in turbulent pipe flow. *J. Fluid Mech.* **608**, 81-112.

Yang, X. I. A. & Griffin, K. P. 2020 Grid point and time step requirements for wall-resolved large-eddy simulation and direct numerical simulation of a developing turbulent boundary layer. arXiv:2010.15307.

Yang, X. I. A., Park, G. I. & Moin, P. 2017 Log-layer mismatch and modeling of the fluctuating wall stress in wall-modeled large-eddy simulations. *Phys. Rev. Fluids* **2**, 104601.

Yang, X. I. A., Sadique, J., Mittal, R. & Meneveau, C. 2015 Integral wall model for large eddy simulations of wall-bounded turbulent flows. *Phys. Fluids* **27**, 025112.